Understanding Slow Deformation Before Dynamic Failure

G. Ventura, S. Vinciguerra, S. Moretti, P.G. Meredith, M.J. Heap, P. Baud, S.A. Shapiro, C. Dinske, and J. Kummerow

Abstract Slow deformation and fracturing have been shown to be leading mechanisms towards failure, marking earthquake ruptures, flank eruption onsets and landslide episodes. The common link among these processes is that populations of microcracks interact, grow and coalesce into major fractures. We present (a) two examples of multidisciplinary field monitoring of characteristic "large scale" signs of impending deformation from different tectonic setting, i.e. the Ruinon landslide (Italy) and Stromboli volcano (Italy) (b) the kinematic features of slow stress perturbations induced by fluid overpressures and relative modelling; (c) experimental rock deformation laboratory experiments and theoretical modelling investigating slow deformation mechanisms, such stress corrosion crack growth. We propose an interdisciplinary unitary and integrated approach aimed to:

(1) transfer of knowledge between specific fields, which up to now aimed at solve a particular problem; (2) quantify critical damage thresholds triggering instability onset; (3) set up early warning models for forecasting the time of rupture with application to volcanology, seismology and landslide risk prevention.

Keywords Stromboli volcano · Landslides

Introduction

Slow deformation and fracturing are the leading mechanisms towards failure episodes, such as earthquake ruptures, flank eruptions and landslides (e.g., Scholtz 1968; Cruden 1974; Varnes 1989; Kilburn and Voight 1998; Brehm and Braile 1999; Di Giovambattista and Tyupkin 2001; Kilburn 2003). Field observations routinely monitor the slow deformation and accelerating seismic event rates that precede macroscopic failure of the crust. Laboratory experiments allow to relate applied stress and the evolution of crack damage by describing the microcrack interaction, growth and coalescence into major fractures (Heap et al. 2009). Theoretical modelling of field (Shapiro et al. 2007) and laboratory data (Main 2000) has been proposed to interpret the observed patterns. Hereafter we present data from two selected sites (Ruinon landslide, Alps, and Stromboli volcano, Italy) where multidisciplinary monitoring networks run. We first show how remotely acquired data by SAR interferometry and seismic arrays can be used to monitor deformation processes in different volcanic settings. We then report data from fluid-induced microseismicity and laboratory investigations that allow us to better understand the physical processes (e.g. crack growth and interaction) that generally proceed larger scale failure events like earthquakes, landslides, and volcanic eruptions and sector collapses.

G. Ventura (✉)
Department of Seismology and Tectonophysics, Istituto Nazionale di Geofisica e Vulcanologia, 00143 Roma, Italy
e-mail: ventura@ingv.it

T. Beer (ed.), *Geophysical Hazards*, International Year of Planet Earth,
DOI 10.1007/978-90-481-3236-2_14,

Monitoring Sites

Ruinon Landslide

A landslide is a mass of rock, debris, or earth, which moves down a slope due to gravity (Cruden 1991). Despite this simple definition, a landslide is a complex phenomenon (Cruden and Varnes 1996). It is characterized by five fundamental mechanisms of movement (fall, topple, slide, spread, and flow) and their combinations. Landslides can occur on material that can range in size and consistency from hundreds of millions of cubic meters of solid rock to single particles of earth or debris. The rate of movement ranges from imperceptible creeping (velocity $<10^{-10}$ m/s) to catastrophic failures (velocity >10 m/s), while the material can move as a whole like a solid block or can flow like a fluid, depending on the water content and other factors. In addition, landslide activity can vary in space and through time and even between different parts of the same displaced mass.

Here, a rather new specific application to a landslide site is described, the synthetic aperture radar (SAR). SAR data are collected by a ground-based radar system forming the synthetic aperture by the sliding of the antennas on a linear rail. Coherent SAR processing converts the raw data into a complex image. The phase of each image pixel contains information on the target sensor distance and can be exploited as a ranging tool. The interferometric technique (InSAR), based on the comparison between paired and coherent SAR images taken at different times, gives extremely precise quantitative information of displacement, thus allowing the monitoring of the morphological changes. One of the main applications of synthetic aperture radar (SAR) interferometry (InSAR) is the monitoring of natural hazards, in particular of those phenomena producing ground displacements such as landslides.

In this specific case we considered a large rockslide in the Italian Alps, where the presence of an independent monitoring system allowed us to validate the results through "ground truth" measurements.

The Ruinon landslide is one of the most hazardous slope movements in the Italian Alps (Fig. 1). The word ruinon literally means "huge ruin" this name gives the idea that the area has been unstable since the past. It is located in Valfurva (Middle Valtellina), near the village of Bormio, in the Rhaetian Alps on the hydrographic right of the Frodolfo stream. The landslide has a continuous movements affecting an estimated volume of rock of 30 million m^3, representing a serious threat to human lives and socioeconomic activities in the area. Its rapid collapse would destroy the road connecting Bormio and Santa Caterina Valfurva and, furthermore, would block the Frodolfo stream, with the consequent formation of a highly unstable landslide dam.

The landslide is located in the lower portion of a southwest-facing slope, with an average inclination of 36°. The slope consists of pre-Permian metapelites (phyllites), belonging to the Upper Austroalpine basement of the Campo-Ortles Nappe, and glacial deposits and debris produced by rock falls locally cover it. The landslide, which has a total length of 770 m and a

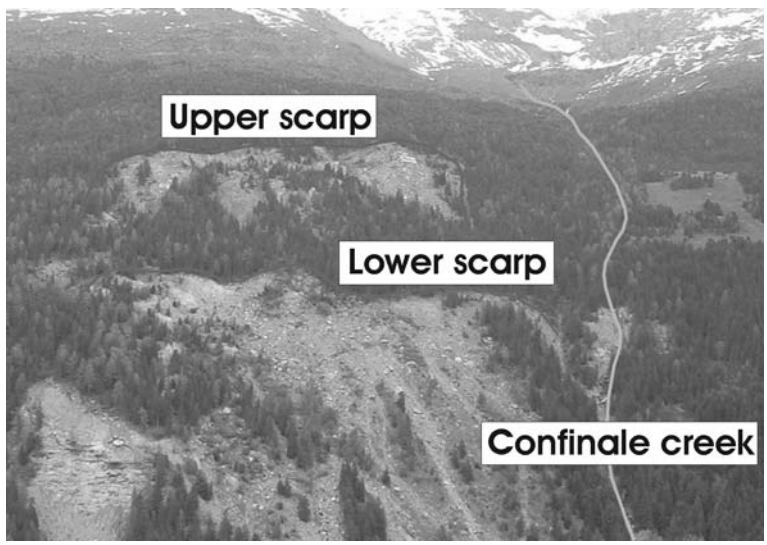

Fig. 1 Aerial picture of the Ruinon rock slide

width of 410 m, is characterized by two main scarps northwest southeast oriented, parallel to the main fracture system (Fig. 2). The "upper scarp" is located at an elevation of 2,100 m above sea level (asl), the "lower scarp" at 1,900 m asl. The Confinale creek, a right hand tributary of the Frodolfo, the course of which is controlled by a northeast-southwest master joint, abruptly cuts the southeastern border of the landslide.

Figure 3 shows the geological section of the area and gives a possible interpretation of the landslide geometry and movement mechanism. Four deep (120 m) boreholes, equipped with inclinometers, were done to determine the section. The data from boreholes show the presence of weak and cataclastic zones at a depth of more than 90 m. The system employed is a portable SAR device known as Linear SAR (LISA),

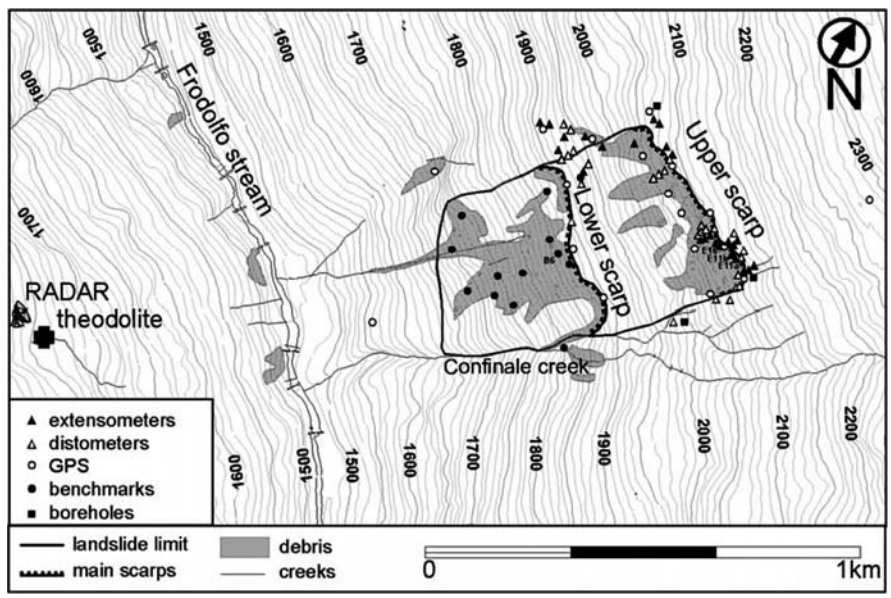

Fig. 2 General plan showing the main geomorphic elements and the location of monitoring instrumentation. The position of the radar is also shown. Labels E11a, E11b, E16, and B6 indicate the sensor used for data validation

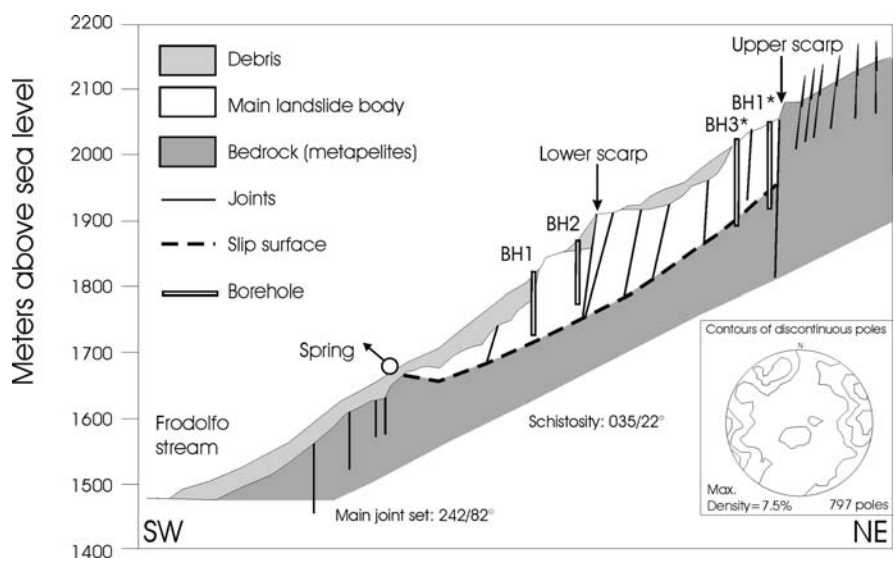

Fig. 3 Interpretative cross section with a hypothesis of the landslide geometry

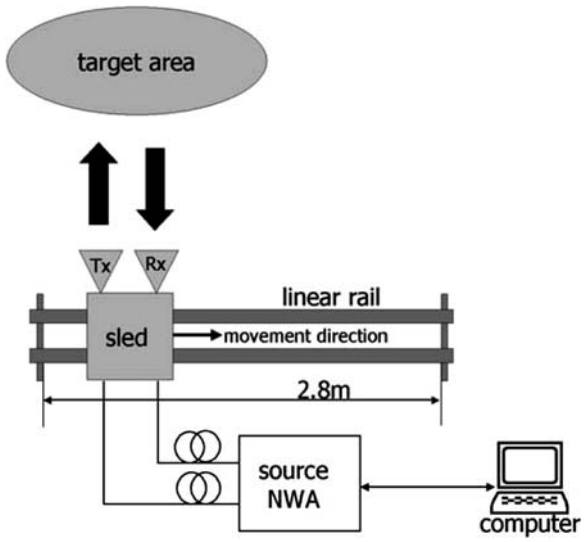

Fig. 4 Scheme of the hardware components of the linear SAR (LISA). Tx, transmitting antenna; Rx, receiving antenna; and NWA, network analyzer

specifically designed and implemented by the Joint Research Centre, Ispra, Italy, for infield use. A scheme of the hardware is provided in Fig. 4. The microwave component of the system is composed of a continuous wave, stepped-frequency scatterometer based on a network analyzer which includes a signal source from 30 kHz to 6 GHz.

An additional module from coherent up-and-down frequency conversion allows measurements in the frequency band from 14 to 18 GHz. The antenna synthesis is obtained by moving a motorized sled, hosting the antennas and other microwave components, along a 2.8 m long linear rail system (Rudolf et al. 1999; Rudolf and Tarchi 1999).

SAR power images of the landslide and a coherence map was produced and a direct comparison with the optical image was done showing a close correlation between areas of higher radar backscattering with areas without vegetation cover. The two main scarps and the Confinale stream, on the left flank of the landslide, were clearly distinguishable too (Tarchi et al. 2003).

The results have been validated by using independent measurements provided by the Geological Monitoring Centre of the Lombardia Region (Fig. 5). The observed displacement patterns obtained by radar and by extensometers (E11a, E11b, and E16) on the upper scarp, confirm the activity of the southeastern portion of the upper scarp, already documented by past monitoring data, whereas the large displacements recorded at the lower scarp were only hypothesized on the basis of geomorphic evidences but had never been assessed quantitatively. In the specific case of the Ruinon landslide the technique allowed us to derive multitemporal displacement maps showing the LOS deformation field of the landslide and providing an immediate indication of the state and distribution of activity.

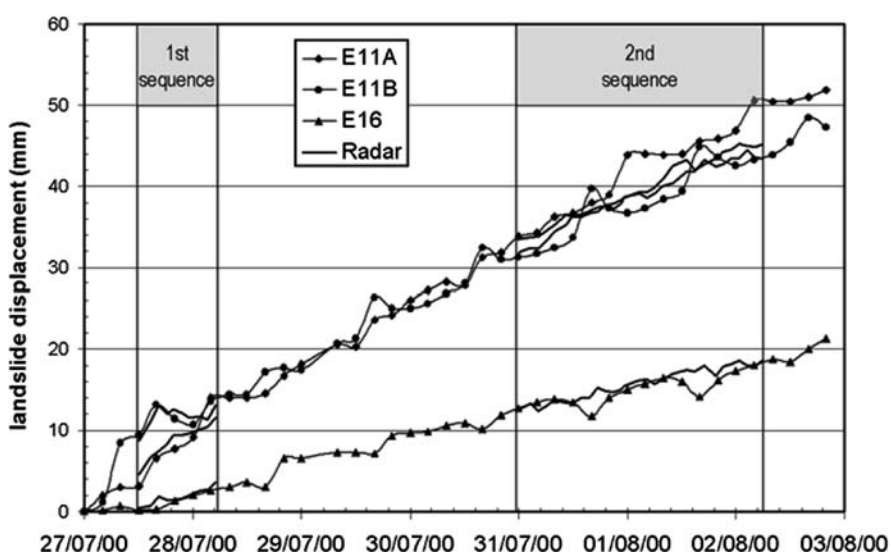

Fig. 5 Cumulated displacements assessed by radar and by extensometers E11a, E11b, and E16 on the upper scarp

Stromboli Volcano

Stromboli Island (924 m asl) is the northernmost volcano of the Aeolian Islands (Southern Italy) and is characterized by a persistent explosive activity over the last 1,400–1,800 years (Rosi et al. 2000). Each episode consists of "strombolian" events every 10–20 min and is associated with streaming of gas from the summit craters (output ~6–12× 10^2 t/day (Allard et al. 1994)). Following Chouet et al. (2003), the gas slug responsible for the explosions form at 220–260 m beneath the summit craters. The persistent activity is periodically interrupted by more energetic explosions (paroxysms), which consist of shortlived blasts fall and ballistic ejecta that reach several hundreds of meters from the craters. One or two events of this type occur per year and the erupted material sometimes affects the two villages on the coast (Barberi et al. 1993). Lava emissions occur about every 10–20 years.

From a structural point of view, magma emissions develops from a NE-SW elongated conduit feeding the three summit craters, which are also NE-SW aligned (Fig. 6). The craters are located at the top of the Sciara del Fuoco (SDF) depression, a morphological expression of sector collapses. This depression, which dip towards NW, is filled with loose deposits (Tibaldi 2001).

Since the summer of 2002, Strombolian activity from the summit craters have shown increased intensity. On 28 December 2002, the magma overflowed, accompanied by an eruptive fissure propagating laterally towards NE. This fissure marked the onset of the effusive eruption, and the end of strombolian activity. On 30 December 2002, a sector of Sciara del Fuoco collapsed, reaching the coastline (Pompilio 2003). The landslide involved a volume of 3 10^7 m^3 and consisted of a submarine and subaerial episodes. The subaerial landslide generated a tsunami, with waves reaching 5–8 meters (Bonaccorso et al. 2003). A vent was

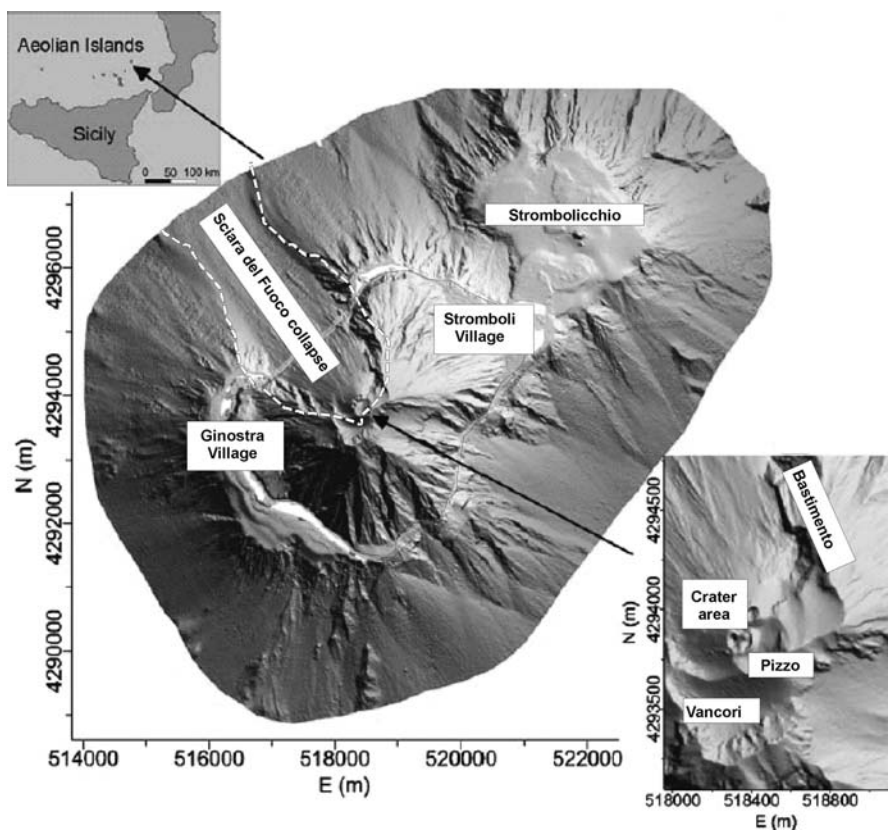

Fig. 6 Digital terrain model of Stromboli Island and offshore with location of the crater area and Sciara del Fuoco collapse (modified from Baldi et al. 2008)

formed between 30 December 2002 and 1 January 2003 within the collapsed area, at 470 m asl. The magma supply decreased in early February, reaching a temporary minimum around mid-February (Ripepe et al. 2005). On 15 February 2003, the NW-SE fissure ended its activity followed by ash emissions from the summit craters occurred. On 3 April 2003, an explosion occurred from the summit crater. This was followed, on 5 April 2003 , by a paroxysm producing pyroclastic density currents and fall deposits (Fig. 7). Strombolian activity at the summit craters resumed after the end of the effusive activity (21 July 2003) (Acocella et al. 2006).

Thus, strombolian activity poses a severe hazard to the population. It is therefore particularly important to understand how magma emplacement and landslides occur at Stromboli and its possible impact. The present-day Istituto Nazionale di Geofisica e Vulcanologia monitoring network at Stromboli include thermal, infrared, and conventional cameras, broadband and short period seismic and acoustic emission

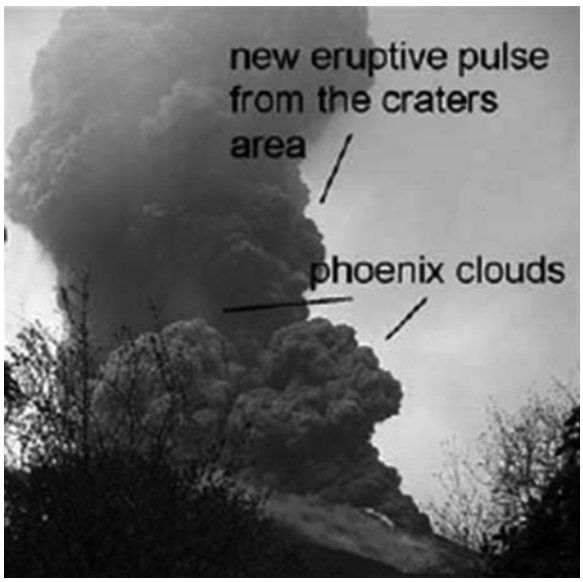

Fig. 7 Picture of the April 5 paroxysm (modified from Rosi et al. 2006)

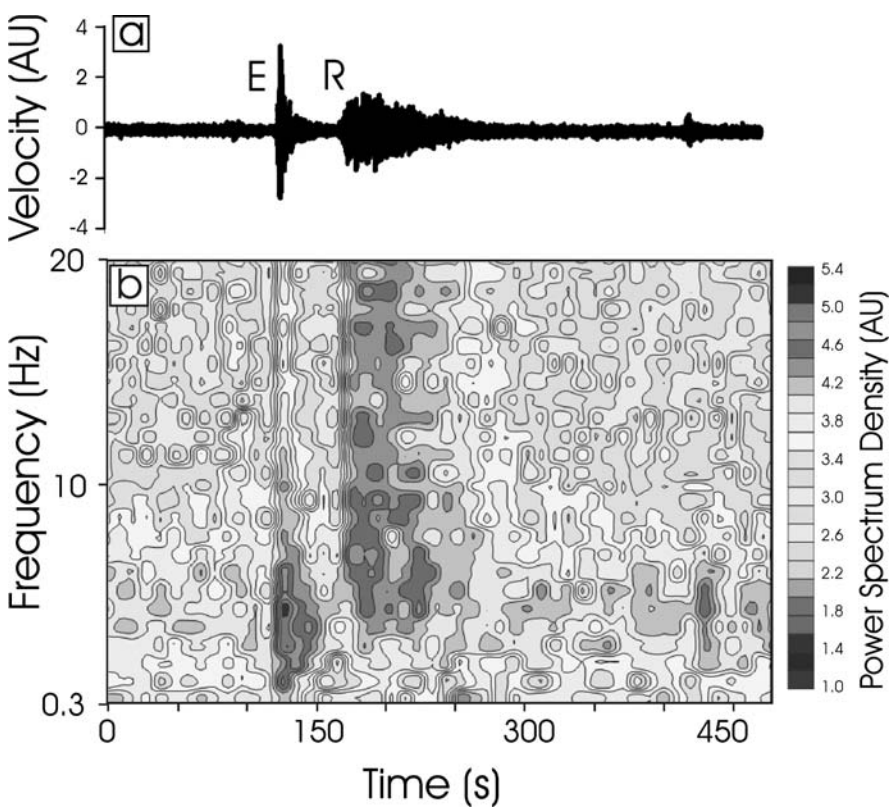

Fig. 8 (a) Seismogram and (b) relative spectrogram of a time series recorded at the vertical component of STR8 on 27 August 2004. An explosion quake (E) shortly precedes a rockfall episode (R) (modified from Falsaperla et al. 2006)

sensors, spectrometers for the detection of SO_2 flux, gravimetric, magnetic, GPS and clinometric networks. The CO_2 flux, the water and gas chemistry are also monitored (http://www.ingv.it and related pages).

According to Falsaperla et al. (2006), the 30 December 2002 landslides represent the only major collapse episodes instrumentally recorded at Stromboli. The seismic monitoring with permanent stations close (<2 km) to the summit craters and Sciara del Fuoco has highlighted minor episodes of flank instability throughout and well after the 2002–2003 lava effusion. Landslides, rockfalls, and debris flows have a typical seismic signature, which allows distinguishing these signals from earthquakes and explosion quakes. An example of time series and relative spectrogram of an explosion shortly preceding a rockfall episode is shown in Fig. 8. Besides the diverse waveform, the relatively brief (30 s) signature of the explosion quake differs strongly from the long (>100 s) duration of the rockfall. The spectrogram analysis highlights the different frequency content of each transient event also with respect to volcanic tremor, i.e., the continuous background signal recorded at Stromboli. The long-term seismic and video monitoring of Stromboli (Falsaperla et al. 2006) suggests that (a) the beginning of a remodeling process of the unstable sectors of the collapsed area after 2002, and (b) the enlargement of the head scarp between 2002 and 2004 involved a negligible rock volume. Nevertheless, if the sliding reach the rim of the crater, this might change the eruptive behavior owing to the asymmetric depressurization of the northwestern portion of the cone. As a result, the AE monitoring of the Sciara del Fuoco collapse is of primary importance for the detection of creep-like signals possibly related to the early phases of sliding episodes.

Kinematic Features and Magnitudes of Fluid Induced Seismicity : Case Studies and Their Interpretation

Sometimes fluid injections are characterized by a risk to induce a seismic event of a significant magnitude. Here we address magnitude distribution of seismicity induced by borehole fluid injections. Firstly we give a short introductory review of microseismicity interpretation in geothermic reservoirs by hydraulic fracturing. Then, we introduce a simple theoretical model, which predicts the earthquake magnitude distributions for fluid injection experiments. The temporal distribution of microearthquake magnitudes depends on the injection pressure, the size of the borehole injection section, the hydraulic diffusivity of rocks, and is also inherited from the statistics of pre-existing crack/fracture systems controlling the local seismicity. We consider different case studies and show how our model can be used to optimise the design of fluid injection experiments and reduce their seismic risk.

In the following, we give a short review of recent research toward establishing physical fundamentals for microseismic investigations of borehole fluid injections. Experiments with borehole fluid injections are typical for exploration and development of hydrocarbon and geothermal reservoirs. The fact that fluid injection causes seismicity has been well-established for several decades. Current on going research is aimed at quantifying and control of this process (Shapiro et al. 2006a, b, 2007).

The fluid induced seismicity covers a wide range of processes between two in the following described asymptotic situations. In liquid-saturated rocks with low to moderate permeability the phenomenon of microseismicity triggering by borehole fluid injections is often related to the pore pressure diffusion. Fluid induced seismicity typically shows then several diffusion specific features, which are directly related to the rate of spatial grow-, to the geometry-, and to the spatial density of microseismic clouds.

Another extreme is the hydraulic fracturing of rocks. Propagation of a hydraulic fracture is accompanied by creation of a new fracture volume, fracturing fluid loss and its infiltration into reservoir rocks as well as diffusion of the injection pressure into the pore space of surrounding rocks and inside the hydraulic fracture. Some of these processes can be seen from features of spatio-temporal distributions of the induced microseismicity. Especially, the initial stage of fracture volume opening as well as the back front of the induced seismicity starting to propagate after termination of the fluid injection can be well identified.

Here, we describe main quantitative features of the both types of induced microseismicity, where triggering is controlled by the pore pressure diffusion and by

the process of new volume opening in the rocks. We also address also magnitude distribution of seismicity induced by borehole fluid injections. Evidently, this is an important question closely related to seismic risk of injection site.

Pore Pressure Diffusion Controlled Seismicity

If the injection pressure (i.e., the bottom hole pressure) is less than the minimum principal stress, then, at least in the first approximation, the behaviour of the seismicity triggering in space and in time is controlled by the process of linear relaxation of stress and pore pressure perturbations initially created at the injection source.

The spatio-temporal features of the pressure-diffusion induced seismicity can be found in a very natural way from the triggering front concept (Shapiro et al. 2002). At a given time t it is probable that events will occur at distances, which are smaller or equal to the size of the relaxation zone (i.e., a spatial domain of significant changes) of the pore pressure. The events are characterised by a significantly lower occurrence probability for larger distances. The surface separating these two spatial domains is the "triggering front." In a homogeneous and isotropic medium the triggering front has the following form:

$$r = \sqrt{4\pi Dt} \tag{1}$$

where t is the time elapsed from the injection start, D is the hydraulic diffusivity and r is the radius of the triggering front (which is a sphere in a homogeneous isotropic medium). Because a seismic event is much more probable in the relaxation zone than at larger distances, Eq. (1) corresponds to the upper bound of the cloud of events on a plot of r versus t (see Fig. 9).

If the injection stops at time t_0 then the earthquakes gradually stop to occur. For times larger then t_0 a surface can be defined which describes propagation of a maximal pore pressure perturbation in the space. This surface (also a sphere in homogeneous isotropic rocks) separates the spatial domain which is still seismically active from the spatial domain (around the injection point) which is already seismically quiet. This surface has been firstly described in (Parotidis et al. 2004) and termed "back front" of induced seismicity:

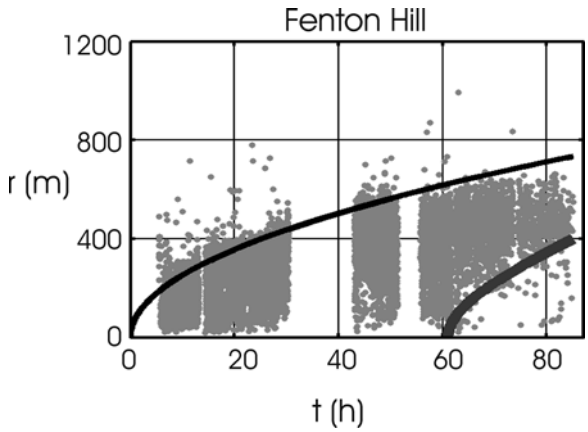

Fig. 9 Fluid-injection induced microseismicity at Fenton Hill (data courtesy of Michael Fehler). Grey points – r-t plot of induced microseismic events (the black line is a triggering front; the grey line is a back front)

$$r_{bf} = \sqrt{2dDt\left(\frac{t}{t_0} - 1\right)\ln\frac{t}{t - t_0}}. \tag{2}$$

Here d is the dimension of the space where the pressure diffusion occurs. The back front is often observed on real data and provides estimates of hydraulic diffusivity consistent with those obtained from the triggering front (see Fig. 9).

Hydraulic Fracturing Controlled Seismicity

During the hydraulic fracturing a fluid is injected through a perforated domain of a borehole into a reservoir rock under the bottom pressure larger than the minimum principal stress. In order to understand the main features of the induced seismicity by such an operation we apply a very simple and rough approximation of the process of the fracture growth resulting from a volume balance for a straight planar (usually vertical – this is the case for the real-data example given here) fracture confined in the reservoir layer. This is the so-called PKN model known from the theory of hydraulic fracturing (Economides and Nolte 2003, pp. 5-1–5-14). Basically, the half-length r of the fracture (which is assumed to be symmetric in respect to the borehole) is approximately given as a function

of the injection time t by the following expression:

$$r = \frac{Q_I t}{4\, h_f C_L \sqrt{2t} + 2\, h_f w}. \quad (3)$$

where Q_I is an injection rate of the treatment fluid, C_L is a fluid-loss coefficient, h_f is a fracture height and w is a fracture width. The first term in the denominator describes the fluid loss from the fracture into surrounding rocks. It is proportional to $\sqrt{t}$ and has a diffusion character. The second term, $2\, h_f w$, represents the contribution of the effective fracture volume and depends mainly on the geometry of the fracture vertical cross-section. In the case of hydraulic fracturing of a formation with a very low permeability (e.g., tight gas sandstones) the fracture body represents the main permeable channel in the formation. The propagating fracture changes in its vicinity the effective stress and activates mainly slip events in the critical fracture systems existing in surrounding rocks (Rutledge and Phillips 2003).

During the initial phase of the hydraulic fracture growth the process of the fracture opening is dominant. This can often lead to a linear expansion with time of the triggering front. If the injection pressure drops the fracture will close. A new injection of the treatment fluid leads to reopening of the fracture, and thus, to a repeated linear propagation of the triggering front. A long term fluid injection leads to domination of diffusion processes. The growth of the fracture slows down and becomes approximately proportional to $\sqrt{t}$. After termination of the fluid injection the seismicity is mainly triggered by the process of the pressure relaxation in the fractured domain. Correspondingly, the back front of the induced microseismicity can be observed, which is described by the Eq. (2) with d= 1 (i.e., approximately, a 1-D diffusion along the hydraulic fracture). Figure 10 shows an example of data demonstrating all the mentioned features of the induced seismicity during hydraulic fracturing.

Magnitudes of Induced Seismicity

Sometimes fluid injections are characterized by a risk to induce a seismic event of a significant magnitude. The magnitudes M of the stimulated seismicity are usually in the range − 3 < M < 2. Nevertheless, especially

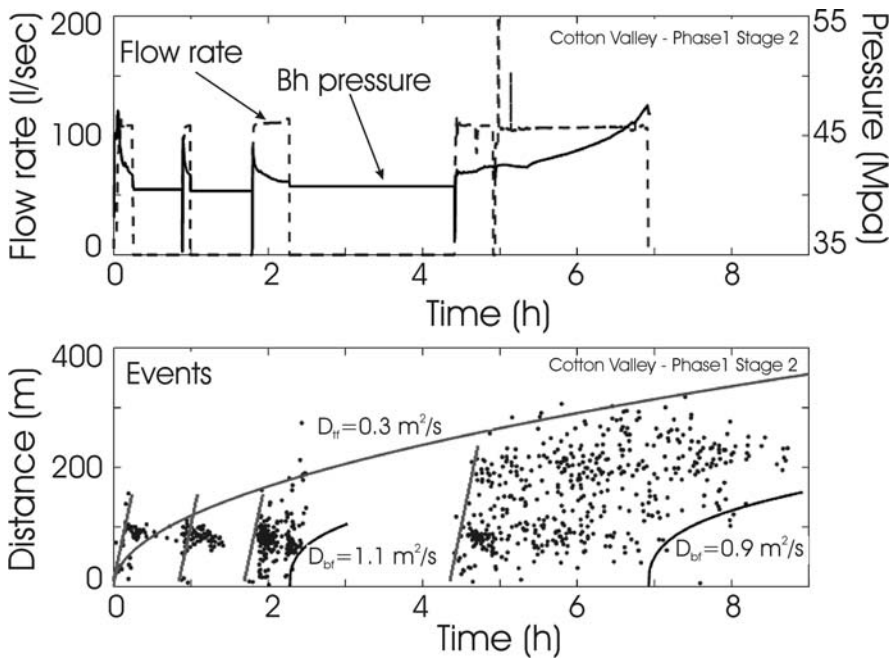

Fig. 10 Hydraulic fracturing induced microseismicity at the Carthage Cotton Vally gas field (data courtesy of James Rutledge). Top: Borehole pressure (measured at the injection domain) and fluid flow rate. Bottom: r-t plot of induced microseismic events (the parabolic grey line – a diffusion type approximation of the triggering; two other parabolic (black) lines – back fronts; straight (grey) lines – fracture opening and reopening and correspondingly, linear with time triggering fronts propagation)

for long-term injections with durations of m onths or even years, earthquakes with larger magnitudes (M = 4 or even larger) have been observed (Majer et al. 2007). So far, little effort has been undertaken to estimate the probability for these events to occur. Here we present a model which allows to calculate the expected number of events with a magnitude larger than a given magnitude value M. It also enables us to identify the main factors which affect the magnitude probabilities.

A basic assumption made here is that the seismicity is induced by pore pressure relaxation in a homogeneous medium, where the hydraulic diffusivity is independent of position and time. For simplicity we also assume a point source for the injection and a constant injection pressure. Wether or not an earthquake occurs on a pre-existing crack depends on the pore pressure and the criticality of the crack (Rothert and Shapiro (2007)). We define the critical value C for a crack as the pore pressure necessary to induce slip along the crack according to the Coulomb failure criterion. The criticality C usually spans several order of magnitudes. Typical ranges are 0.001–1 MPa (see Rothert and Shapiro (2007) and Brodsky et al. (2000)). Note, that a higher value of C means that the crack is more stable. We define n as the density of statistically homogeneously distributed pre-existing cracks. We furthermore consider a fluid injection, which starts at time $t = 0$ and has a constant strength q (which is proportional to the injection pressure and has physical units of power). Then it can be shown that the total number of events increases linearly with injection time at an event rate of $(qn)/C_{\max}$.

We postulate that the frequency magnitude relation is consistent with the Gutenberg-Richter relationship. In other words, the logarithm of the probability of events with magnitude larger than M is equal to $a - b$M. Here, b is known as the *b value* which is usually close to 1. The number of fluid injection induced events N (M, t) with magnitude larger than M is given by the product of the cumulative event number until injection time t and the probability of an event to have a magnitude larger than M. We finally obtain the following bi-logarithmical relation

$$\log N(\mathrm{M},t) = \log\left(\frac{qt}{F}\right) - b\mathrm{M} + a \qquad (4)$$

We denote the parameter $F = C_{\max}/n$ as tectonic potential of the injection site. This quantity has physical units of energy and characterizes how easy or difficult seismicity can be induced at a particular location. A detailed analysis of Eq. (4) indicates that the number of earthquakes of magnitudes greater than a given one increases with the duration of the injection, the injection pressure, the flow rate and the borehole radius. It also depends on the hydraulic diffusivity and the crack concentration divided by the maximumcritical pore pressure.

We compare the number of events as a function of time as predicted by our formulation (Eq. 4) with observations from data sets at injection sites in Japan (Ogachi geothermic site). During an experiment at Ogachi geothermic site in 1991, a volume of more than 10,000 cubic meters of water was injected at a depth of 1,000 m into hard rock (granodiorite). The pressure remained relatively stable throughout the experiment (Fig. 11). A microseismic event cloud of about 500 m thickness and 1,000 m length with nearly 1,000 detected events was stimulated (Kaieda et al. 1993). The magnitudes were determined by measuring velocity amplitudes and alternatively seismogram oscillation durations (Kaieda and Sasaki 1998).

Magnitude statistics were biased by the performance of the observation system and processing in the magnitude ranges M <− 2.5 and M > − 1.5.

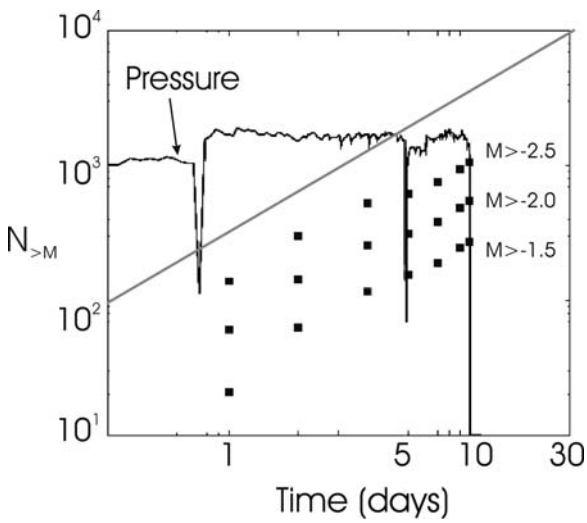

Fig. 11 Data of the Ogachi 1991 borehole injection experiment. The squares are observed cumulative numbers of earthquakes with a magnitude large than the indicated one as a function of injection time (bi-logarithmic plot). The straight line shows the theoretically predicted (see Eq. 4) proportionality coefficient 1. Shown is also the injection pressure as a function of time

When the injection pressure is close to constant, the $N(M, t)$ functions are nearly linear in the bilogarithmic plot. The steps between lines corresponding to different magnitudes M are regularly distributed and time-independent. These two prominent observations are as predicted by our model (Eq. 4). The steps between the lines can be used to estimate the *b value*. In 1993 an injection into two open borehole sections at different depth levels was performed at Ogachi injection site. The magnitude distributions exhibit a similar behaviour as for the experiment in 1991 (not shown here).

The magnitude distributions observed in Fig. 11 agree quite well with the predictions of Eq. 4, which postulates a linear relation between $\log N(M, t)$ and $\log t$.

Spatio-temporal dynamics of microseismic clouds contributes to characterization of hydraulic properties of reservoirs and to monitoring and description of hydraulic fractures. For example, *r-t*-plots show signatures of fracture volume growth, of fracturing fluid loss, as well as of diffusion of the injection pressure into rocks and inside the fracture. Diffusion controlled triggering is often observed at geothermic reservoirs. New volume creation controlled triggering is usually observed at hydraulic fracturing of tight gas reservoirs.

We have furthermore considered a poroelastic medium with randomly distributed sub-critical cracks obeying a Gutenberg-Richter statistics. Based on that we have derived a simple theoretical model, which predicts the earthquake magnitude distributions for fluid injection experiments. The temporal distribution of microearthquake magnitudes depends on the injection pressure, the size of the borehole injection section, the hydraulic diffusivity of rocks, and is also inherited from the statistics of pre-existing crack/fracture systems controlling the local seismicity. Our parametrization can be used to optimize the design of fluid injection experiments and reduce their seismic risk.

Experimental Study of Brittle Creep in Crustal Rocks

The understanding of slow, time-dependent crack growth is crucial to unraveling the complexities of the evolution and dynamics of the brittle crust. The presence of cracks allows the crust to store and transport fluids, and even modest changes in crack size, density or linkage can produce major changes in fluid transport properties. Time-dependent rock deformation therefore has both a scientific and a socio-economic impact since it exerts a key influence on the precursory phase of important geo-hazards such as earthquake rupture and volcanic eruption.

The majority of rocks forming the Earth's crust, even those at depth, contain microporosity comprising some or all of open pores between grains, triple-junction voids between crystalline phases, grain boundary voids and open microcracks. Water and other aqueous solutions are ubiquitous in the upper crust, and below a few hundred metres these void spaces in most rocks are saturated. The presence of a fluid phase not only affects the mechanical behaviour of rock, but also allows chemical rock-fluid interactions to occur. In a purely mechanical sense, a pressurized pore fluid acts to reduce all the applied normal stresses and thus allows rocks to fail at lower differential stress than would otherwise be the case (Terzaghi 1943; Jaeger et al. 2007). Chemically, aqueous solutions affect the deformation of rock in two main ways: (1) they act to weaken the rock via the reduction of surface free energy as the result of the absorption of pore fluid onto the internal pore surfaces (Orowan 1944; Rehbinder 1948; Andrade and Randall 1949), and (2) they also weaken rocks by promoting subcritical crack growth, of which stress corrosion is considered the most important mechanism under upper crustal conditions (Anderson and Grew 1977; Atkinson 1984; Atkinson and Meredith 1987; Costin 1987). Under these conditions, the (intensified) stress concentration (K) at crack tips that is responsible for crack growth is known to be a function of both applied stress (σ_a) and crack length (c) (e.g. Lawn 1993; Paterson and Wong 2005). Hence, since the relationship between the crack growth velocity (V) and K is very non-linear, the crack growth rate will accelerate as the cracks extends leading eventually to dynamic failure (Fig. 12). However, the majority of experimental data on stress corrosion cracking has been derived from experiments on single cracks at ambient pressure, and few data exist on the bulk behaviour of rock containing a population of cracks. Nevertheless it has been hypothesized that, for bulk rock deforming in a brittle manner under triaxial stress conditions, stress corrosion will lead to highly non-linear time-dependent deformation (Main et al. 1993;

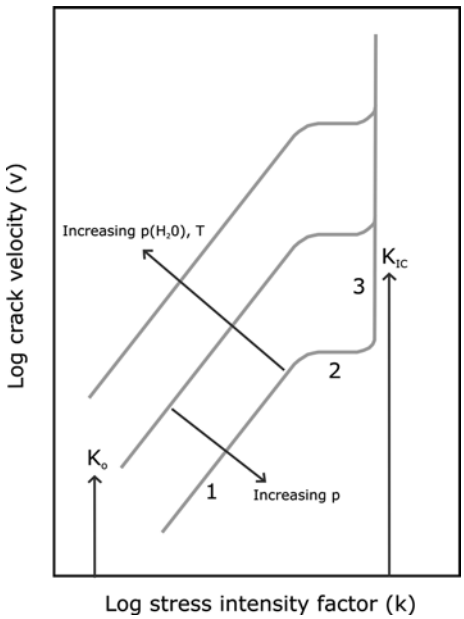

Fig. 12 Schematic stress intensity factor (K)/crack velocity (V) diagram for subcritical tensile crack growth due to stress corrosion. K_o – the stress corrosion crack growth limit; K_{IC} – the critical stress intensity factor or fracture toughness; p – effective confining pressure; p (H_2O) – pore fluid pressure; T – temperature

Main 2000). This allows rocks to deform even under a constant applied differential stress over extended periods of time; a phenomenon known as brittle creep (or static fatigue in the engineering literature). This style of deformation has conventionally been described as exhibiting an apparent trimodal behaviour when axial strain is plotted against time (commonly known as a *creep curve*). The three stages of the creep curve have conventionally been described as; (1) primary or decelerating creep, (2) secondary or steady-state creep, and (3) tertiary or accelerating creep (as illustrated in Fig. 13).

Here we present illustrative results from an experimental study of brittle creep in sandstone under triaxial stress conditions. The experiments were performed at room temperature in the servo-controlled 400 MPa triaxial rock deformation apparatus in the Rock & Ice Physics Laboratory (RIPL) at University College London (Fig. 14a). The internal sample assembly is shown in Fig. 14b. During all experiments, axial strain was measured continuously using LVDT displacement transducers, and pore volume change was measured continuously using a servo-controlled pore fluid pressure intensifier and volumometer (Benson et al. 2007). Microseismicity in the form of acoustic emission (AE) was recorded continuously via ten piezo-electric transducer crystals embedded within the rubber. The measurement of axial strain, pore volume change and the output of acoustic emission (AE) energy during experiments is important because all three parameters are considered as proxies for the accumulation of crack damage during deformation, as previously demonstrated by and Baud and Meredith (1997).

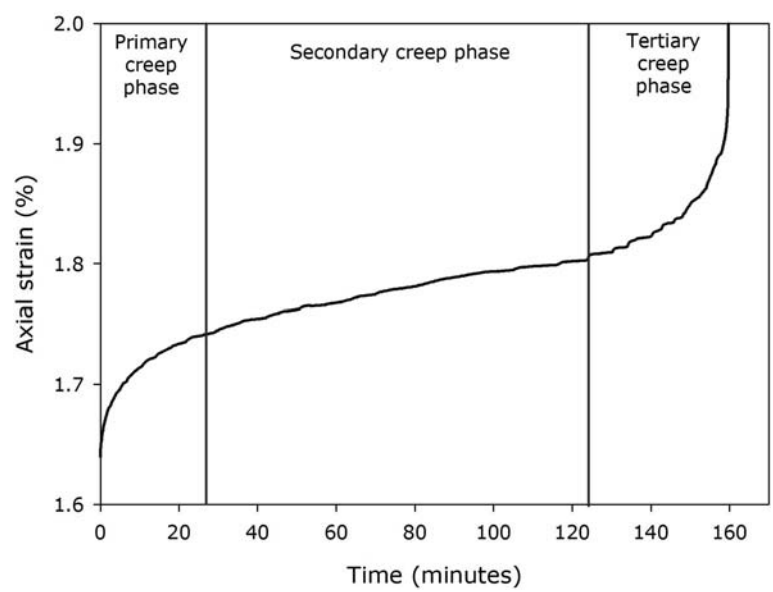

Fig. 13 The classic trimodal creep curve for brittle material at a constant applied differential stress. The curve shows the three stages of brittle creep (1) primary or decelerating (2) secondary or steady-state and (3) tertiary or accelerating creep. The secondary creep phase is where creep strain rates are calculated

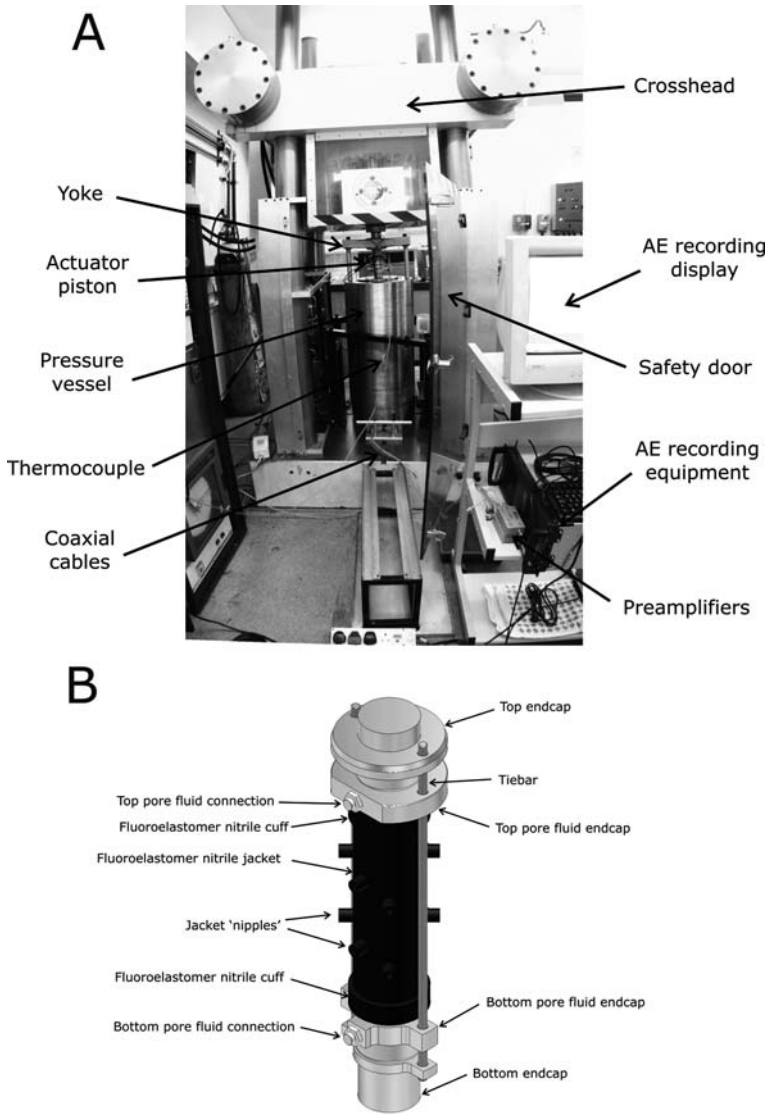

Fig. 14 (a) Photograph of the servo-controlled 400 MPa triaxial rock deformation apparatus at the Rock & Ice Physics Laboratory, UCL (b) three-dimensional Autodesk Inventor picture of the jacketed sample setup

Prior to performing brittle creep experiments, it is necessary to perform constant strain rate experiments to establish the short-term failure characteristics of the test material. Once this has been established, brittle creep experiments can then performed under the same effective stress conditions. In creep experiments, samples are first loaded to a pre-determined percentage of the peak stress (or strength) established during the constant strain rate experiments. Generally, following Baud & Meredith (1997), this is in the range 80–90% of the short-term strength. After this preloading, samples are allowed to deform under constant effective differential stress until failure. The evolution of crack damage is monitored throughout each experiment by measuring the damage proxies of axial strain, pore volume change and output of AE energy. At the end of each experiment, creep strain rates are calculated from the secondary phase of the creep curve.

Figure 15 shows the stress-strain curve and the damage proxies of pore volume change and cumulative AE energy for a constant strain rate experiment on a sample of Darley Dale sandstone conducted at an effective confining pressure of 30 MPa and a strain rate of 1.0×10^{-5} s^{-1}. Following an initial period of compaction, the onset of dilatancy occurs at a

differential stress of around 40 MPa. As expected, this also corresponds to the onset of AE output around 0.5% axial strain. The minimum in the pore volume change curve marks the transition from compaction-dominated deformation to dilatancy-dominated deformation (which we term D′), and occurs at a differential stress around 130 MPa. The peak stress was 160 MPa.

A series of constant stress brittle creep experiments were then performed on samples of Darley Dale sandstone over a range of constant applied differential stress levels in order to yield times-to-failure and creep strain rates over several orders of magnitude (Heap et al. 2009). Following Baud and Meredith (1997), the levels of applied differential stress were selected to be greater than that corresponding to the onset of dilatancy (C′), but lower than the stress level that would generate very rapid failure within a few seconds or a few minutes. Such stress levels generally corresponded to between 80 and 90% of the peak stress in short-term constant strain rate experiments (Fig. 15).

Figure 16 shows the results of one such experiment (from Heap et al. 2009) conducted at a constant effective differential stress of 132 MPa (85% of the peak stress). The three independent proxy measures of damage (axial strain, pore volume change and cumulative AE energy) are also shown plotted against time. The axial strain curve shows the trimodal behaviour via which creep deformation has generally been interpreted. The primary creep phase is characterized by an initially high strain rate that decreases with time to reach a linear secondary phase that is often interpreted as steady-state creep. After an extended period of time, a tertiary phase is entered, characterized by accelerating strain. This eventually results in macroscopic failure of the samples by propagation of a shear fault. The two other damage proxies of pore volume change and cumulative AE energy also exhibit trimodal behaviour. In particular, the tertiary creep phase is characterized by accelerations in all three proxies for damage. Creep strain rates were calculated for all experiment in the series from the linear portions of the strain-time curves. These are shown in Fig. 17, plotted as a function of differential stress. The data demonstrate that the creep strain rate depends strongly and non-linearly on the level of applied differential stress. Even modest changes in applied stress results in order of magnitude changes in creep strain rate. For example, at 141 MPa (90% of peak stress), the creep strain rate was 3.6×10^{-6} s^{-1} and the time-to-failure was approximately 10 min. At 132 MPa (85% of peak stress; Fig.

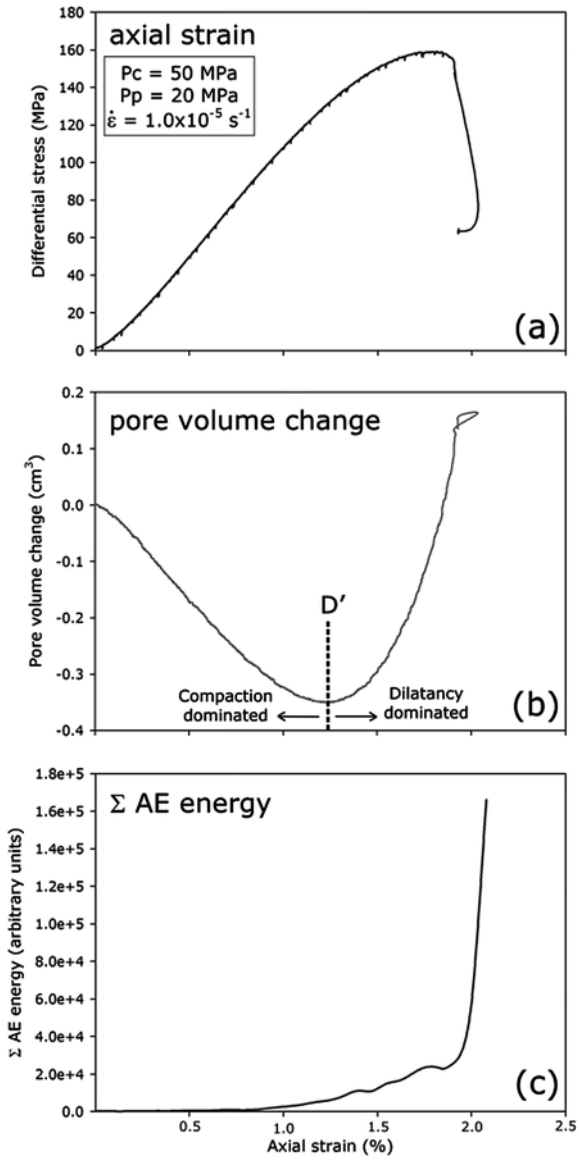

Fig. 15 Conventional constant strain rate experiment on a water-saturated sample of Darley Dale sandstone showing variability in the three proxies for damage within the rock: (a) stress-strain curves, (b) the pore volume change curves and (c) the AE energy output curves. Experimental conditions are indicated on the figure. D′, the stress at which a dilatant-dominated regime dominates, is indicated in (b). Pc – confining pressure; Pp – pore fluid pressure

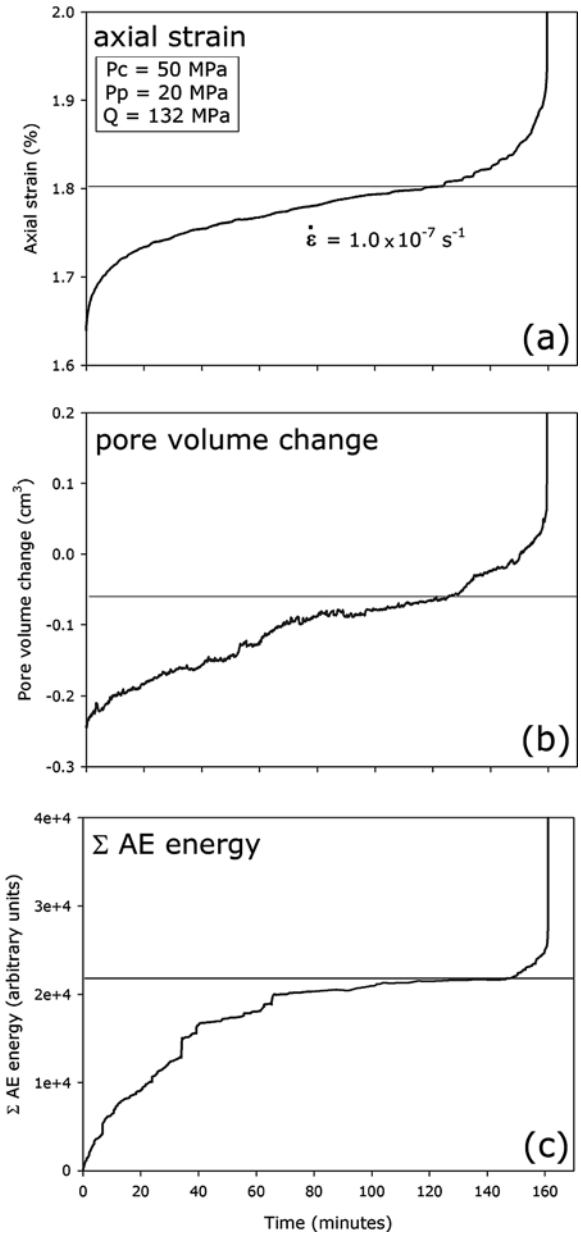

Fig. 16 Graphs of the three damage proxies for a conventional brittle creep experiment on water-saturated Darley Dale sandstone that yielded a creep strain rate of 1.0×10^{-7}. (a) time-strain (creep) curve (b) pore volume change curve and (c) output of AE energy. The position of the onset of accelerating tertiary creep is indicated in each figure by a horizontal line. Experimental conditions are indicated on the figures. Pc – confining pressure; Pp – pore fluid pressure; Q – applied differential stress

16), the creep strain rate decreased to 1.0×10^{-7} s^{-1} and the time-to-failure increased to 160 min (2.6 h). At the lowest stress of 125 MPa (80% of peak stress), the creep strain rate was 1.3×10^{-8} s^{-1} and the time-to-failure was 3,600 min (60 h). In summary, a 10% reduction in applied differential stress resulted in a decrease in creep strain rate and an increase in time-to-failure of approximately 2.5 orders of magnitude.

Furthermore, we also observe that all three measured proxies for crack damage (axial strain, pore volume change and output of AE energy) have approximately equal values at the onset of tertiary creep in all experiments, even though the creep strain rates vary over about three orders of magnitude. This implies that there is a critical level of damage required before the onset of acceleration to failure. The observation of a critical damage threshold has previously been proposed in a number of experimental studies (Griggs 1939, 1940; Wawersik and Brown 1973; Cruden 1974; Kranz and Scholz 1977; Baud and Meredith 1997) and has also been predicted by modelling (e.g., Armitrano and Helmstetter 2006). Kranz & Scholz (1977) suggested that the tertiary creep phase will not commence until the rock has sustained a critical amount of inelastic volumetric strain. More recently, in creep experiments on sandstone, Baud and Meredith (1997) showed that not only was the onset of tertiary creep marked by a critical level of strain, but that it was also marked by critical levels of AE energy output and change in damage volume.

More recently, mean-field theories of damage mechanics have been developed (e.g., Lockner 1998; Main 2000) that invoke a two-stage, rather than a three-stage creep process: (1) a phase of strain hardening involving distributed crack damage, followed by (2) a phase of strain softening involving crack interaction and coalescence. It is proposed that phase (1) dominates in the early stage of deformation and phase (2) dominates in the later stage of deformation. Such as models also therefore postulate a critical damage threshold, where crack interaction leads to a rapid acceleration to failure on a localized fault plane. As the stress intensity at crack tips is influenced by the lengths of the cracks, given suitable conditions, the non-linear relation between strain rate and stress given by stress corrosion theory means that the rate at which a crack grows can accelerate even under a constant boundary stress. For a population of cracks growing in a rock sample held at constant stress, this process is embodied by accelerating strain rate and AE emission with time.

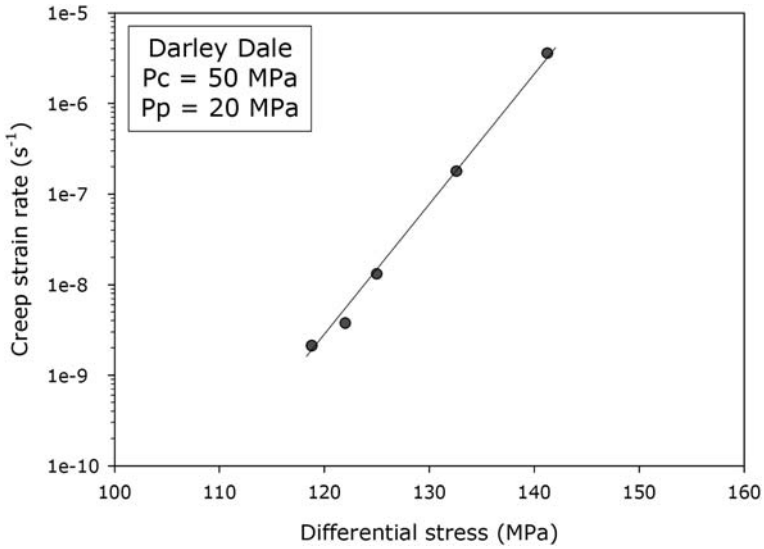

Fig. 17 Creep strain rate data from multiple conventional brittle creep experiments on water-saturated Darley Dale sandstone plotted on a log scale against applied differential stress. Experimental conditions are displayed on the figure. Pc – confining pressure; Pp – pore fluid pressure

Proposal Objectives and Conclusions

Natural hazards such earthquakes, volcanic eruptions and landslides are a severe and permanent threat to human life and sustainable economic development. Dynamic ruptures are preceded by slow deformation mechanisms, in which fractures extend by the growth and coalescence of smaller cracks. Understanding the slow deformation mechanisms preceding dynamic failure is thus a crucial goal to design innovative strategies for forecasting seismic, volcanic and landslide behaviour. Advances towards this goal strongly depend on developing a better comprehension of the flow and fracture behaviour of rocks on various scales in space and time. In order to do so a large range of skills needs to be developed and applied, from a deep fundamental understanding of the physical processes involved up to their monitoring and crisis management.

At the field scale a multidisciplinary monitoring is now required, aimed to apply new technologies and integrated methodologies to real time monitoring of ground deformation (GPS, SAR, InSAR, clinometry, cameras), seismic and microseismic ruptures (broadband, short period seismic and acoustic emission sensors), along with gravimetric and magnetic networks. In volcanic areas real time monitoring of temperature, gas and fluid chemistry (CO_2 and SO_2) is also required (Infrared cameras, spectrometers for the detection of gas and fluid flux). Thanks to the fast technological developments taking place, new instrumentation and the relative techniques can be potentially utilized for interpreting deformation mechanisms in space and time and to design an alarm and early warning system for civil protection purposes.

In order to achieve this goal a better understanding of the physico-chemical processes controlling slow deformation mechanisms preceding dynamic failure is needed.

Rock deformation laboratory experiments allow determination of how intrinsic properties of rocks (e.g., microstructure, composition, fabric, microcracks, strength, seismic properties and attenuation) vary as a function of extrinsic variables (pressure, temperature, pore fluid pressure, differential stress). Theoretical modelling can validate the experimental observations and can be used to scale the patterns observed in the laboratory to the field scale. In recent years the development of new experimental, analytical and modelling techniques has generated substantial progress. Despite the smaller length and time scale of laboratory experiments compared to nature, field observations can be quantitatively reproduced and modelled, thus significantly contributing to the understanding of the dynamics of tectonic and transport processes. Thanks to laboratory experiments and the work at different length scales (from micro to field scale) is now possible to estimate key parameters such as the strength of the lithosphere.

Environmental monitoring, laboratory experiments, theoretical modelling and hazard assessment has now

reached a stage where further development of any specific field requires a much tighter and active collaboration among various groups of experimentalists, field-scale scientists and theoreticians both from the geological and geophysical communities to upscale from the micro to the field scale the results obtained in the laboratory.

One of the main issues is that current monitoring systems are mostly calibrated for the detection of ruptures ranging at "large scale" from hundred of meters to kilometres, thus they cannot detect slow deformation nucleating at "small scale" (centimetres to tens of meters), which have been therefore defined so far as "silent" process (e.g., Ozawa et al. 2003). The developing and deploying of specific sensors devoted to the "slow deformation" the a tight connection with the know-how from laboratory experiments is needed. Indeed through triaxial rock-deformation experiments is possible to analyse how data comparable to field observations such seismic event rates, seismic wave velocities, and ratios of seismic P- to S-wave velocities evolve with respect carefully simultaneously measured swith mechanical parameters of the rock (e.g., stress, strain and crack damage).

We then propose a new departure based on an interdisciplinary unitary and integrated approach aimed to

(1) transfer of knowledge between specific fields, which up to now aimed at solve a particular problem;
(2) quantify critical damage thresholds triggering dynamic failure;
(3) set up early warning models for forecasting the time of rupture with application to volcanology, seismology and landslide risk prevention.

In order to do so we propose to combine the outcome of two neat examples of multidisciplinary (e.g. remote sensing by SAR interferometry and high frequency sensors for microseismicity) field monitoring of characteristic "large scale" signs of impending deformation from different tectonic setting, i.e. the Ruinon landslide (Italy) and Stromboli volcano (Italy) with the kinematic features of slow stress perturbations induced by fluid overpressures and relative modelling and the results of experimental rock deformation laboratory experiments and theoretical modelling investigating slow deformation mechanisms, such stress corrosion crack growth.

The expected benefits of this approach will allow us to develop new technologies aimed to monitor the "slow deformation" preceding the dynamic failure signals in unstable sectors of the Earth, and will provide invaluable data for theoretical modeling of critical damage thresholds triggering instability onset. This "topic" answers two of the main questions of the Hazards Theme of the International Year of the Planet Earth (http://www.yearofplanetearth.org/), and, in particular, the questions 2 "What technologies and methodologies are required to assess the vulnerability of people and places to hazards – and how might these be used at a variety of spatial scales?" and 3 "How does our current ability to monitor, predict and mitigate vary from one geohazard to another? What methodologies and new technologies can improve such capabilities, and so help civil protection locally and globally?" (Beer 2008, and http://www.yearofplanetearth.org/content/downloads/Hazards.pdf).

Acknowledgments This work has been supported by the sponsors of the PHASE university consortium project. The NEST Pathfinder Program Triggering Instabilities in Materials and Geosystems (contract NEST-2005-PATH-COM-043386) is acknowledged. The microseismic data from the Ogachi site are courtesy of Dr. H. Kaieda (Central Research Institute of Electric Power Industry, Japan). Help and assistance of Dr. T. Ito (Institute of Fluid Science, Tohoku) is greatly appreciated. This paper is related to the project "Creep" accredited by the Hazards Theme of IYPE.

References

Acocella V, Neri M, Scarlato P (2006) Understanding shallow magma emplacement at volcanoes: orthogonal feeder dikes during the 2002–2003 Stromboli (Italy) eruption. Geophys Res Lett. DOI:10.1029/2006GL026862

Allard P, Carbonelle J, Metrich N, Loyer H, Zattwoog P (1994) Sulfur output and magma degassing budget of Stromboli volcano. Nature 368:326–330

Amitrano D, Helmstetter A (2006) Brittle creep damage and time to failure in rocks. J Geophys Res. DOI:10.1029/2005JB004252

Anderson OL, Grew PC (1977) Stress corrosion theory of crack propagation with applications to geophysics. Rev Geophys 15:77–104

Andrade EN, Randall RFY (1949) The Rehbinder effect. Nature 164:1127

Atkinson BK (1984) Subcritical crack growth in geological materials. J Geophys Res 89:4077–4114

Atkinson BK, Meredith PG (1987) The theory of subcritical crack growth with applications to minerals and rocks. In:

Atkinson BK (ed) Fracture Mechanics of Rock. Academic Press, London
Baldi P, Coltelli M, Fabris M, Marsella M, Tommasi P (2008) High precision photogrammetry for monitoring the evolution of the NW flank of Stromboli volcano during and after the 2002–2003 eruption. Bull Volcanol 70:703–715
Barberi F, Rosi M, Sodi A (1993) Volcanic hazard assessment at Stromboli based on review of historical data. Acta Volcanol 3:173–187
Baud P, Meredith PG (1997) Damage accumulation during triaxial creep of Darley Dale sandstone from pore volumometry and acoustic emission. Int J Rock Mech Min Sci 34:3–4
Beer T (2008) Minimising risk maximising awareness: the hazards theme of the international year of the planet Earth. 33IGC Oslo 2008 PEH01204L 105 Abstract volume
Benson PM, Thompson AB, Meredith PG, Vinciguerra S, Young RP (2007) Imaging slow failure in triaxially deformed Etna basalt using 3D acoustic-emission location and X-ray computed tomography. Geophys Res Lett. DOI:10.1029/2006GL028721
Bonaccorso A, Calvari S, Garfi' G, Lodato L, Patane D (2003) Dynamics of the December 2002 flank failure and tsunami at Stromboli volcano inferred by volcanological and geophysical observations. Geophys Res Lett. DOI:10.1029/2003GL017702
Brehm DJ, Braile LW (1999) Intermediate-term earthquake prediction using the modified time-to-failure method in South California. Bull Seis Soc Am 89:275–293
Brodsky EE, Karakostas V, Kanamori H (2000) A new observation of dynamically triggered regional seismicity: earthquakes in Greece following the August 1999 Izmit Turkey earthquake. Geophys Res Lett 27:2741–2744
Chouet B, Dawson P, Ohminato T, Martini M, Saccorotti G, Giudicepietro F, De Luca G, Milana G, Scarpa R (2003) Source mechanisms of explosions at Stromboli Volcano Italy determined from moment-tensor inversions of very-long-period data. J Geophys Res. DOI:10.1029/2002JB001919
Costin LS (1987) Time-dependent deformation and failure. In: Atkinson BK (ed) Fracture Mechanics of Rock. Academic Press, London
Cruden DM (1974) Static fatigue of brittle rock under uniaxial compression. Int J Rock Mech Min Sci 11:67–73
Cruden DM (1991) A simple definition of a landslide. Bull Int Assoc Eng Geol 43:27–29
Cruden DM, Varnes DJ (1996) Landslides types and processes. In: Land-slides: Investigation and Mitigation. Transportation Research Board, National Research Council, National Academies Press, Washington DC
Di Giovambattista R, Tyupkin YS (2001) An analysis of the process of acceleration of seismic energy emission in laboratory experiments on destruction of rocks and before strong earthquakes on Kamchatka and in Italy. Tectonophysics 338: 339–351
Economides MJ, Nolte KG (2003) Reservoir Stimulation. Wiley, Chichester
Falsaperla S, Neri M, Pecora E, Spampinato S (2006) Multidisciplinary study of flank instability phenomena at Stromboli volcano Italy. Geophys Res Lett. DOI:10.1029/2006GL025940
Griggs D (1939) Creep of Rocks. J Geol 47:225–251
Griggs D (1940) Experimental flow of rocks under conditions favouring recrystallization. Bull Seis Soc Am 51:1001–1022
Heap M, Baud JP, Meredith PG, Bell AF, Main IG (2009) Time-dependent brittle creep in Darley Dale sandstone. J Geophys Res 114, B07203, doi:10.1029/2008JB006212.
Jaeger JN, Cook GW, Zimmerman R (2007) Fundamentals in Rock Mechanics (4th Edition). Blackwell Publishing, London
Kaieda H, Kiho K, Motojima I (1993) Multiple fracture creation for hot dry rock development. Trends Geophy Res 2:127–139
Kaieda H, Sasaki S (1998) Development of fracture evaluation methods for Hot Dry Rock geothermal power – Ogachi reservoir evaluation by the AE method. CRIEPI report U97107 (in Japanese with English abstract)
Kilburn CRJ (2003) Multiscale fracturing as a key to forecasting volcanic eruptions. J Volcanol Geotherm Res 125:271–289
Kilburn CRJ, Voight B (1998) Slow rock fracture as eruption precursor at Soufriere Hills volcano: Montserrat. Geophys Res Lett 25:3665–3668
Kranz R, Scholz CH (1977) Critical dilatant volume of rocks at the onset of tertiary creep. J Geophys Res 82:4893–4898
Lawn B (1993) Fracture of Brittle Solids. Cambridge University Press, Cambridge
Lockner D (1998) A generalized law for brittle deformation of Westerly granite. J Geophys Res 103:5107–5123
Main IG (2000) A damage mechanics model for power-law creep and earthquake aftershock and foreshock sequences. Geophys J Int 142:151–161
Main IG, Sammonds PR, Meredith PG (1993) Application of a modified Griffith criterion to the evolution of fractal damage during compressional rock failure. Geophys J Int 115: 367–380
Majer EL, Baria R, Stark M, Oates S, Bommer J, Smith B, Asanuma H (2007) Induced seismicity associated with enhanced geothermal systems. Geothermics 36:185–222
Orowan E (1944) The fatigue of glass under stress. Nature 154:341–343
Ozawa S, Miyazaki S, Hatanaka Y, Imakiire T, Kaidzu M, Murakami M (2003) Characteristic silent earthquakes in the eastern part of the Boso peninsula Central Japan. Geophys Res Lett. DOI:10.1029/2002GL016665
Parotidis M, Shapiro SA, Rothert E (2004) Back front of seismicity induced after termination of borehole fluid injection. Geophys Res Lett. DOI:10.1029/2003GL018987
Paterson MS, Wong TF (2005) Experimental Rock Deformation – The Brittle Field. Springer, New York
Pompilio M (2003) Eruzione Stromboli 2002–2003: Cronologia dell'eruzione localizzazione e migrazione delle bocche eruttive. Internal report Ist Naz di Geofis e Vulcanol Catania, Italy
Rehbinder PA (1948) Hardness Reducers in Drilling (Translated from Russian). CSIR, Melbourne
Ripepe M, Marchetti E, Ulivieri G, Harris AJL, Dehn J, Burton M, Caltabiano T, Salerno G (2005) Effusive to explosive transition during the 2003 eruption of Stromboli volcano. Geology 33:341–344
Rosi M, Bertagnini A, Harris AJL, Pioli L, Pistolesi M, Ripepe M (2006) A case history of paroxysmal explosion at Strom-

boli: timing and dynamics of the April 5 2003 event. Earth Planet Sci Lett 243:594–606

Rosi M, Bertagnini A, Landi P (2000) Onset of the persistent activity at Stromboli volcano (Italy). Bull Volcanol 62: 294–300

Rothert E, Shapiro SA (2007) Statistics of fracture strength and fluid – induced microseismicity. J Geophys Res. DOI:10.1029/2005JB003959

Rudolf H, Leva D, Tarchi D, Sieber AJ (1999) A mobile and versatile SAR system. Int Geosc Rem Sens Symp, Hamburg

Rudolf H, Tarchi D (1999) LISA: the linear SAR instrument. Tech Rep I 99 126 Eur Comm Joint Res Cent, Ispra

Rutledge JT, Phillips WS (2003) Hydraulic stimulation of natural fractures as revealed by induced microearthquakes Carthage Cotton Valley gas field east Texas. Geophysics 68:441–452

Shapiro SA, Dinske C, Kummerow J (2007) Probability of a given magnitude earthquake induced by a fluid injection. Geophys Res Lett. DOI:10.1029/2007GL031615

Shapiro SA, Dinske C, Rothert E (2006a) Hydraulic-fracturing controlled dynamics of microseismic clouds. Geophys Res Lett. DOI:10.1029/2006GL026365

Shapiro SA, Kummerow J, Dinske C, Asch G, Rothert E, Erzinger J, Kümpel HJ, Kind R (2006b) Fluid induced seismicity guided by a continental fault: injection experiment of 2004/2005 at the German deep drilling site (KTB). Geophys Res Lett. DOI:10.1029/2005GL024659

Shapiro SA, Rothert E, Rath V, Rindschwentner J (2002) Characterization of fluid transport properties of reservoirs using induced microseismicity. Geophysics 67: 212–220

Scholz CH (1968) The frequency–magnitude relation of microfracturing in rock and its relation to earthquakes. Bull Seismol Soc Am 58:399–415

Tarchi D, Casagli N, Moretti S, Leva D, Sieber AJ (2003) Monitoring landslide displacements using groung-based synthetic aperture radar interferometry: application to the Ruinon landslide in the Italian Alps. J Geophys Res. DOI:10.1029/2002JB002204

Terzaghi K (1943) Theoretical Soil Mechanics. John Wiley and Sons, New York

Tibaldi A (2001) Multiple sector collapses at Stromboli volcano Italy: how they work. Bull Volcanol 63:112–125

Varnes DJ (1989) Predicting earthquakes by analyzing accelerating precursory seismic activity. Pageoph 130: 661–686

Wawersik WR, Brown WS (1973) Creep Fracture in Rock. Utah University, Department of Mechanical Engineering, Salt Lake City